Inorganic Chemistry

Article

pubs.acs.org/IC

Controlling the Electronic States and Physical Properties of MMX-Type Diplatinum-Iodide Chain Complexes via Binary Countercations

Hiroaki Iguchi,*[,†,§] Shinya Takaishi,[†] Brian K. Breedlove,[†] Masahiro Yamashita,*[,†] Hiroyuki Matsuzaki,[‡,∥] and Hiroshi Okamoto[‡]

[†]Department of Chemistry, Graduate School of Science, Tohoku University, 6-3 Aza-aoba, Aramaki, Sendai 980-8578, Japan

[‡]Department of Advanced Materials Science, Graduate School of Frontier Sciences, The University of Tokyo and CREST (JST), Kashiwa 277-8561, Japan

Supporting Information

ABSTRACT: MMX-type quasi-one-dimensional iodide-bridged dinuclear Pt complexes (MMX chains) with binary countercations show a new alternating charge-polarization + charge-density-wave (ACP+CDW) electronic state and reversible switching of the electronic states and physical properties upon dehydration and rehydration process. By comparing several MMX chains with various binary countercations with previous chains, we found that the short backbone of the aliphatic diammonium ion was indispensable for realizing the ACP+CDW state because it induces a 2-fold periodicity along the chain axis via twisting of the ligands. Moreover, the reversibility of the changes in the structure and electrical conductivity upon dehydration and rehydration depend on the length of aliphatic diammonium ion. Short diammonium ions support a robust framework, which undergoes reversible structural changes. On the other hand, long and bent aliphatic diammonium ions weaken the framework, which causes partial degradation of the crystal and a decrease in the electrical conductivity when the structure changes. However, the decrease in the activation energy of the electrical conductivity after the dehydration process is independent of the robustness of the complex, indicating that the orbital overlap in MMX chains with binary countercations increases upon dehydration. Controllable electronic states and physical properties provide a platform for designing the multifunctional materials based on MMX chains.

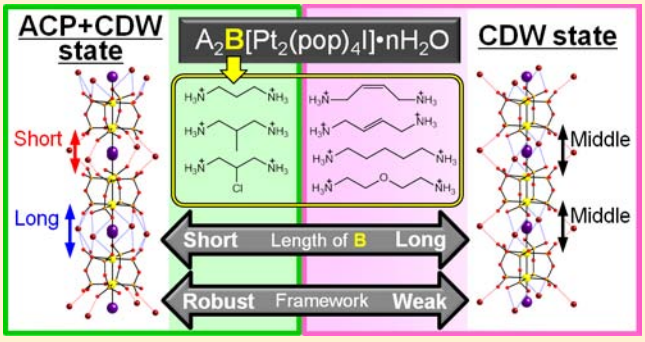

INTRODUCTION

One-dimensional (1D) electron systems exhibit various electronic states, which have unique physical properties, such as high conductivity,[1] large optical nonlinearity,[2,3] Luttinger liquid behavior,[4] and ultrafast optical responses.[5] The energy of the electronic states depends on the competition or cooperation among various factors, such as electron−phonon interaction, coulomb repulsion, and transfer integral, and these relationships stabilize various electronic states in these systems.

Quasi-1D (Q1D) halogen-bridged metal complexes can be used to study the chemistry and physics of 1D electron systems since the energetic factors can be tuned easily by changing their components, such as metals, bridging halogens, in-plane ligands, and counterions. Moreover, the ease of preparing single crystals enables us to discuss their electronic states in detail on the basis of their structures, whereas it is impossible to obtain single crystals of other 1D materials, such as π-conjugated organic polymers and carbon nanotubes.

Q1D halogen-bridged metal complexes are categorized into two groups by the number of metal ions per unit: MX chains are mononuclear complexes bridged infinitely by a halide ion, that is, ····M—X—M—X····, and MMX chains are paddle-wheel type dinuclear complexes bridged infinitely by a halide ion, that is, ····M-M—X—M-M—X····. The 1D electron system of these complexes consists of the d_{z^2} orbitals of the metal ions (M) and the p_z orbitals of the bridging halide ions (X). MX chains have interesting physical properties, such as gigantic third-order nonlinear optical properties,[3] midgap absorptions attributable to solitons and polarons,[6] and charge-density-wave (CDW) to Mott-Hubbard (MH) phase transitions.[7] However, in MX chains, only CDW and MH states have been found to be stable ground states. In comparison with MX chains, the higher degrees of freedom of the electrons in MMX chains increase the competition and/or cooperation among several energetic factors, giving rise to a larger variety of electronic states with small energy gaps among them.[8] On the basis of theoretical calculations and experimental data, the electronic states of the MMX chains have been classified into the following four states:

(a) average-valence (AV) state

$$-M^{2.5+}-M^{2.5+}-X-M^{2.5+}-M^{2.5+}-X-$$

(b) charge-density-wave (CDW) state

Received: July 6, 2012
Published: September 4, 2012

   dx.doi.org/10.1021/ic301469u | Inorg. Chem. 2012, 51, 9967−9977

$\cdots M^{2+}-M^{2+}\cdots\cdots X-M^{3+}-M^{3+}-X\cdots$

(c) charge-polarization (CP) state

$\cdots M^{2+}-M^{3+}-X\cdots\cdots M^{2+}-M^{3+}-X\cdots$

(d) alternating charge-polarization (ACP) state

$\cdots M^{2+}-M^{3+}-X-M^{3+}-M^{2+}\cdots\cdots X\cdots$

These electronic states are strongly correlated to the position of the bridging halide ion. Except in the AV state, the bridging halide ion is close to the M^{3+} ion. Strictly, formal oxidation numbers, 3+ and 2+, should be represented as $(3-\delta)$+ and $(2+\delta)$+, respectively. The AV state is a Robin–Day class III system, whereas the other three are class II systems.[9] Because each electronic state exhibits various physical properties, MMX chains have the potential to be multifunctional switching materials.

MMX chains synthesized to date are classified into two categories on the basis of their ligands: a dithioacetate (dta) system, $[M_2(RCS_2)_4I]$ (M = Ni, and Pt; R = alkyl chain group),[10,11] and a diphosphite (pop) system, $Y_4[Pt_2(pop)_4X]\cdot nH_2O$ and $Y'_2[Pt_2(pop)_4X]\cdot nH_2O$ (Y = alkali metal, alkyl ammonium, etc.; Y′ = alkyldiammonium; X = Cl^-, Br^-, and I^-; pop = $P_2H_2O_5^{2-}$).[12]

In the dta system, a high conductivity and a metal–insulator transition have been reported.[10] Recently, Zamora et al. have reported the formation of nanowires on a substrate, which is promising for future molecule-based devices.[11] Thus, methods to control the electronic states and accompanying physical properties of MMX chains are needed. However, in the case of dta systems, the adjustable components are limited to the alkyl chain groups that can be introduced onto the dta ligand and metal ions (Ni and Pt). On the other hand, in the case of the pop systems, the negatively charged chains require countercations, of which there are a huge number of possible candidates. Furthermore, removing lattice water molecules should change the electronic states of the MMX chains.[12g–i,13] Therefore, the pop system is a suitable alternative for realizing new electronic states and phase transitions.

Recently, we have reported that MMX chains containing two kinds of countercations (binary countercations), $K_2(H_3NCH_2CHXCH_2NH_3)[Pt_2(pop)_4I]\cdot 4H_2O$ (X = H (**K1·4H$_2$O**), Me (**K2·4H$_2$O**), Cl (**K3·4H$_2$O**))[13,14] are in a new ACP+CDW electronic state and that their electronic states and physical properties can be switched reversibly via dehydration–rehydration. However, the mechanism for the stabilization of the ACP+CDW state and the detailed electronic structure of the ACP+CDW state are unclear.

Herein, we discuss the origin and detailed electronic structure of the ACP+CDW state of **K1·4H$_2$O**–**K3·4H$_2$O** in comparison with MMX chains with aliphatic diammonium ions (B^{2+}) $\mathbf{4}^{2+}$–$\mathbf{7}^{2+}$ (Scheme 1) and alkali metal ions (A^+). In addition, we discuss the characteristics of MMX chains with binary countercations and the effect of the length of the B^{2+} on the dehydration–rehydration process.

Scheme 1. Chemical Structure of Aliphatic Diammonium Ions (B^{2+}) Introduced As One of the Countercations in MMX Chains in This Study

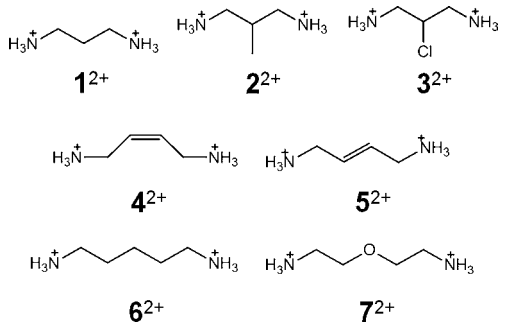

EXPERIMENTAL SECTION

Synthesis. All of the commercially available chemicals were reagent grade and used as received. The starting $Pt(II)_2$ and $Pt(III)_2$ complexes, $K_4[Pt_2(pop)_4]\cdot 2H_2O$ and $K_4[Pt_2(pop)_4I_2]$, respectively, were synthesized from K_2PtCl_4, H_3PO_3, and I_2 following reported procedures.[15] $(Bu_4N)_4[Pt_2(pop)_4]$ and $(Bu_4N)_4[Pt_2(pop)_4I_2]$ were synthesized by using a cation exchange method.[12i,16] $(H_3NC_3H_6NH_3)SO_4$ (**1**SO_4), and $(H_3NC_5H_{10}NH_3)SO_4$ (**6**SO_4) were synthesized by neutralizing the amine with sulfuric acid in ethanol solutions. **K1·4H$_2$O**–**K3·4H$_2$O**,[13,14] $(H_3NCH_2CHMeCH_2NH_3)Cl_2$ (**2**Cl_2),[14] $(H_3NCH_2CHClCH_2NH_3)Cl_2$ (**3**Cl_2),[13,17] *cis*-1,4-diamino-2-butene dihydrochloride (**4**Cl_2),[18] *trans*-1,4-diamino-2-butene dihydrochloride (**5**Cl_2),[18] 3-oxapentane-1,5-diamine dinitrate (**7**$(NO_3)_2$)[19] were synthesized as previously reported. Elemental analyses were performed at the Research and Analytical Center for Giant Molecules, Graduate School of Science, Tohoku University.

K_2(4)[Pt_2(pop)$_4$I]·4H$_2$O (K4·4H$_2$O). Aqueous solutions of the Pt_2 complexes (containing 6.2 mM $K_4[Pt_2(pop)_4]\cdot 2H_2O$ and 5.4 mM $K_4[Pt_2(pop)_4I_2]$), **4**Cl_2 (100 mM), and KNO_3 (400 mM) were mixed in a volume ratio of 11:1:10 and allowed to stand for 2 days. **K4·4H$_2$O** was obtained as glossy brown cubic crystals. Anal. Calcd for $C_4H_{28}IK_2N_2O_{24}P_8Pt_2$: C, 3.61; H, 2.12; N, 2.10. Found: C, 3.75; H, 2.01; N, 1.99. Yield: 66.5%

K_2(5)[Pt_2(pop)$_4$I]·4H$_2$O (K5·4H$_2$O). Synthetic procedure for **K5·4H$_2$O** was similar to that of **K4·4H$_2$O**, except that **5**Cl_2 (100 mM) was used. Glossy brown cubic crystals were obtained. Anal. Calcd for $C_4H_{28}IK_2N_2O_{24}P_8Pt_2$: C, 3.61; H, 2.12; N, 2.10. Found: C, 3.91; H, 1.84; N, 2.12. Yield: 68.7%

K_2(6)[Pt_2(pop)$_4$I]·4H$_2$O (K6·4H$_2$O). Aqueous solutions of the Pt_2 complexes (containing 6.2 mM $K_4[Pt_2(pop)_4]\cdot 2H_2O$ and 5.4 mM $K_4[Pt_2(pop)_4I_2]$), **6**SO_4 (100 mM), and KNO_3 (200 mM) were mixed in the volume ratio of 6:1:5 and left in the refrigerator for 2 days. **K6·4H$_2$O** was obtained as glossy brown crystals with $Pt(II)_2$ complex, $(\mathbf{6})_2[Pt_2(pop)_4]$, as a minor component. Anal. Calcd for $C_5H_{32}IK_2N_2O_{24}P_8Pt_2$: C, 4.46; H, 2.39; N, 2.08. Found: C, 4.46; H, 2.30; N, 2.02. Yield: 72.9%

K_2(7)[Pt_2(pop)$_4$I]·4H$_2$O (K7·4H$_2$O). Synthetic procedure for **K7·4H$_2$O** was similar to that for **K4·4H$_2$O**, except that **7**$(NO_3)_2$ (100 mM), KNO_3 (200 mM) was used and that the volume ratio was 4:1:3. Glossy brown crystals were obtained. Anal. Calcd for $C_4H_{30}IK_2N_2O_{25}P_8Pt_2$: C, 3.56; H, 2.24; N, 2.08. Found: C, 3.70; H, 2.36; N, 2.08. Yield: 95.4%

Rb_2(1)[Pt_2(pop)$_4$I]·4H$_2$O (Rb1·4H$_2$O). Aqueous solutions of the Pt_2 complexes (containing 4.1 mM $(Bu_4N)_4[Pt_2(pop)_4]$ and 4.1 mM $(Bu_4N)_4[Pt_2(pop)_4I_2]$), **1**$SO_4$ (100 mM), Rb_2SO_4 (450 mM), and additional water were mixed in a volume ratio of 1.6:1.5:1:0.7 and allowed to stand for 2 days. **Rb1·4H$_2$O** was obtained as glossy brown cubic crystal. Anal. Calcd for $C_3H_{28}IN_2O_{24}P_8Pt_2Rb_2$: C, 2.55; H, 2.00; N, 1.98. Found: C, 2.45; H, 1.95; N, 1.93. Yield: 51.9%

Rb_2(2)[Pt_2(pop)$_4$I]·4H$_2$O (Rb2·4H$_2$O). Synthetic procedure for **Rb2·4H$_2$O** was similar to that for **Rb1·4H$_2$O**, except that **2**Cl_2 (100 mM) was used and that the volume ratio was 2:1:1:2. Glossy brown cubic crystals were obtained. Anal. Calcd for $C_4H_{30}IN_2O_{24}P_8Pt_2Rb_2$: C, 3.37; H, 2.12; N, 1.96. Found: C, 3.39; H, 2.03; N, 1.90. Yield: 55.1%

Rb_2(3)[Pt_2(pop)$_4$I]·4H$_2$O (Rb3·4H$_2$O). Synthetic procedure for **Rb3·4H$_2$O** is similar to that for **Rb1·4H$_2$O**, except that **3**Cl_2 (100 mM) was used and that the volume ratio was 2:1:1:2. Glossy brown cubic crystals were obtained. Anal. Calcd for $C_3H_{27}ClIN_2O_{24}P_8Pt_2Rb_2$: C, 2.49; H, 1.88; N, 1.94. Found: C, 2.54; H, 1.74; N, 1.93. Yield: 59.6%

dx.doi.org/10.1021/ic301469u | Inorg. Chem. 2012, 51, 9967–9977

Table 1. Crystal Data for K4·4H$_2$O−K7·4H$_2$O and Rb1·4H$_2$O−Rb7·4H$_2$O

	K4·4H$_2$O	K5·4H$_2$O	K6·4H$_2$O	K7·4H$_2$O	Rb1·4H$_2$O	Rb2·4H$_2$O
empirical formula	$C_4H_{28}IK_2N_2O_{24}P_8Pt_2$	$C_4H_{28}IK_2N_2O_{24}P_8Pt_2$	$C_5H_{32}IK_2N_2O_{24}P_8Pt_2$	$C_4H_{30}IK_2N_2O_{25}P_8Pt_2$	$C_3H_{28}IN_2O_{24}P_8Pt_2Rb_2$	$C_4H_{30}IN_2O_{24}P_8Pt_2Rb_2$
formula weight	1331.32	1331.32	1347.37	1349.34	1412.05	1426.08
temperature/K	100(2)	293(2)	100(2)	100(2)	100(2)	100(2)
λ (Mo−Kα)/Å	0.71073	0.71073	0.71073	0.71073	0.71073	0.71073
crystal system	orthorhombic	orthorhombic	orthorhombic	orthorhombic	orthorhombic	tetragonal
space group	*Cmmm*	*Cmmm*	*Pbam*	*Pbam*	*Pnn*2	*P*4*nc*
a/Å	12.326(4)	12.164(2)	12.5503(13)	12.237(2)	12.7396(11)	13.5079(11)
b/Å	14.753(4)	15.175(3)	14.9494(16)	15.432(3)	14.0609(13)	13.5079(11)
c/Å	8.585(3)	8.6247(15)	8.5403(9)	8.5382(15)	17.5723(15)	17.531(2)
V/Å^3	1561.2(8)	1592.0(5)	1602.3(3)	1612.3(5)	3147.7(5)	3198.7(5)
Z	2	2	2	2	4	4
D(calc)/g cm^{-3}	2.832	2.777	2.793	2.779	2.980	2.961
μ(Mo−Kα)/mm^{-1}	10.709	10.501	10.436	10.373	13.430	13.217
F(000)	1250	1250	1270	1270	2620	2652
crystal size/mm^3	0.18 × 0.09 × 0.09	0.18 × 0.13 × 0.11	0.13 × 0.05 × 0.02	0.14 × 0.06 × 0.04	0.13 × 0.06 × 0.04	0.05 × 0.03 × 0.03
no. of total reflections	15800	5882	11101	15274	22304	32516
no. of unique reflections	1047	1060	1957	1984	7183	4056
R_{int}	0.0323	0.0239	0.0292	0.0389	0.0416	0.0653
GOF	1.161	0.952	0.958	1.136	0.839	0.715
*R*1, *wR*2 [$I > 2\sigma(I)$]	0.0170, 0.0499	0.0152, 0.0384	0.0198, 0.0524	0.0308, 0.0654	0.0316, 0.0536	0.0260, 0.0423
*R*1, *wR*2 (all data)	0.0172, 0.0499	0.0158, 0.0385	0.0262, 0.0537	0.0402, 0.0680	0.0540, 0.0570	0.0536, 0.0455
Flack parameter					0.448(2)	0.001(9)
max, min $\Delta\rho$/e$^-$ Å^{-3}	0.870, −0.693	0.414, −0.501	0.865, −0.670	1.563, −0.798	1.378, −1.167	1.910, −1.087

	Rb3·4H$_2$O	Rb4·4H$_2$O	Rb5·2H$_2$O	Rb6·4H$_2$O	Rb7·4H$_2$O
empirical formula	$C_3H_{27}ClIN_2O_{24}P_8Pt_2Rb_2$	$C_4H_{28}IN_2O_{24}P_8Pt_2Rb_2$	$C_4H_{24}IN_2O_{22}P_8Pt_2Rb_2$	$C_5H_{32}IN_2O_{24}P_8Pt_2Rb_2$	$C_4H_{30}IN_2O_{25}P_8Pt_2Rb_2$
formula weight	1446.48	1424.06	1388.01	1440.11	1442.08
temperature/K	250(2)	100(2)	293(2)	100(2)	100(2)
λ (Mo−Kα)/Å	0.71073	0.71073	0.71073	0.71073	0.71073
crystal system	tetragonal	orthorhombic	orthorhombic	orthorhombic	orthorhombic
space group	*P*4*nc*	*Cmmm*	*Cmmm*	*Pbam*	*Cmmm*
a/Å	13.5401(16)	12.360(2)	11.9661(13)	12.630(3)	12.272(4)
b/Å	13.5401(16)	14.891(3)	15.1128(17)	15.101(4)	15.533(5)
c/Å	17.555(3)	8.6936(15)	8.6299(10)	8.655(2)	8.650(3)
V/Å^3	3218.4(8)	1600.1(5)	1560.6(3)	1650.8(7)	1648.8(9)
Z	4	2	2	2	2
D(calc)/g cm^{-3}	2.929	2.956	3.03	2.897	2.905
μ(Mo−Kα)/mm^{-1}	13.217	13.210	13.545	12.807	12.825
F(000)	2576	1322	1322	1342	1342
crystal size/mm^3	0.07 × 0.07 × 0.05	0.04 × 0.03 × 0.02	0.09 × 0.03 × 0.03	0.27 × 0.04 × 0.015	0.14 × 0.05 × 0.04
no. of total reflections	36166	9565	9269	18902	9899
no. of unique reflections	4721	1343	1301	2554	1373
R_{int}	0.0614	0.0950	0.0777	0.0533	0.0913
GOF	0.831	1.141	1.118	0.808	1.004
*R*1, *wR*2 [$I > 2\sigma(I)$]	0.0309, 0.0534	0.0538, 0.1195	0.0307, 0.0728	0.0252, 0.0495	0.0310, 0.0761
*R*1, *wR*2 (all data)	0.0588, 0.0588	0.0629, 0.1234	0.0325, 0.0735	0.0478, 0.0524	0.0348, 0.0772
Flack parameter	0.142(9)				
max, min $\Delta\rho$/e$^-$ Å^{-3}	1.516, −1.487	5.264, −1.439	1.747, −1.349	2.089, −1.008	2.121, −1.130

Rb$_2$(4)[Pt$_2$(pop)$_4$I]·4H$_2$O (Rb4·4H$_2$O). Synthetic procedure for **Rb4·4H$_2$O** is similar to that for **Rb1·4H$_2$O**, except that 4Cl$_2$ (100 mM) was used and that the volume ratio was 7:2:5:7. Glossy brown crystals of **Rb4·4H$_2$O** were obtained as a minor component. Elemental analysis could not be performed because of the formation of several impurities.

Rb$_2$(5)[Pt$_2$(pop)$_4$I]·2H$_2$O (Rb5·2H$_2$O). Synthetic procedure for **Rb5·2H$_2$O** was similar to that for **Rb1·4H$_2$O**, except that 5Cl$_2$ (100 mM) was used and that the volume ratio was 4:1:3:4. Glossy brown crystals were obtained. The number of lattice water molecules were confirmed by a thermogravimetric analysis (TGA) shown in Supporting Information, Figure S1. Anal. Calcd for $C_4H_{24}IN_2O_{22}P_8Pt_2Rb_2$: C, 3.46; H, 1.77; N, 1.98. Found: C, 3.64; H, 1.77; N, 1.98. Yield: 43.8%

Rb$_2$(6)[Pt$_2$(pop)$_4$I]·4H$_2$O (Rb6·4H$_2$O). Synthetic procedure for **Rb6·4H$_2$O** was similar to that for **Rb1·4H$_2$O**, except that 6SO$_4$ (100 mM) was used and that the volume ratio was 3:2:1:1. In addition, the reaction mixture was placed in a refrigerator for 2 days. **Rb6·4H$_2$O** was obtained as glossy brown crystals with (**6**)$_2$[Pt$_2$(pop)$_4$] as a minor component. Anal. Calcd for $C_5H_{32}IN_2O_{24}P_8Pt_2Rb_2$: C, 4.17; H, 2.24; N, 1.95. Found: C, 4.51; H, 2.29; N, 2.07. Yield: 35.5%

Rb$_2$(7)[Pt$_2$(pop)$_4$I]·4H$_2$O (Rb7·4H$_2$O). Synthetic procedure for **Rb7·4H$_2$O** was similar to that for **Rb1·4H$_2$O**, except that 7(NO$_3$)$_2$ (100 mM) was used and that the volume ratio was 2:1:1:2. Glossy

dx.doi.org/10.1021/ic301469u | *Inorg. Chem.* 2012, 51, 9967−9977

brown crystals were obtained. Anal. Calcd for $C_4H_{30}IN_2O_{25}P_8Pt_2Rb_2$: C, 3.33; H, 2.10; N, 1.94. Found: C, 3.41; H, 2.02; N, 1.94. Yield: 81.4%

Dehydration Method. For dehydration, a sample was heated at 70 °C under vacuum (<100 Pa). Electrical conductivity was performed on samples placed under dehydrating conditions until the conductivity stopped changing (typically about 4 h). For X-ray powder diffraction (XRD) measurements, ground samples dehydrated for 1 d were used.

Rehydration Method. A dehydrated sample was placed in a closed box containing water vapor for 1 d. For electrical conductivity measurements, samples attached to a sample stage were placed into the box.

Single-Crystal X-ray Structure Determination. The crystallographic data for MMX chains with binary countercations are summarized in Table 1. Crystallographic information files (CIF) for each complex are included in the Supporting Information. Single-crystal X-ray structural analysis was performed on a Bruker SMART 1000 (50 kV, 30 mA) with graphite-monochromated Mo Kα radiation (λ = 0.7107 Å). Diffraction data were collected in ω-scan steps of 0.3°. Degradation of the crystal by X-ray irradiation was analyzed by comparing the diffraction patterns of the first and last 50 diffraction photographs in same ω range. The temperature was controlled by using a Japan Thermal Engineering DX-CS190LD temperature controller. Diffraction intensities were integrated by using SAINT Software[20] with Lorentz-polarization correction. The crystal structures were solved by using direct methods (SIR97[21] or SHELXS-97[22]), followed by Fourier syntheses. Structure refinement was performed by using full matrix least-squares procedures using SHELXL-97[22] on F^2 in the Yadokari-XG2009 software.[23]

Positional disorders were observed in most complexes. The bridging iodide ions in **K4·4H$_2$O**−**K7·4H$_2$O** and **Rb4·4H$_2$O**−**Rb7·4H$_2$O** and A^+ in **K4·4H$_2$O**, **K5·4H$_2$O**, **Rb4·4H$_2$O**, **Rb5·2H$_2$O**, and **Rb7·4H$_2$O** were disordered. The B^{2+} in **K4·4H$_2$O**−**K7·4H$_2$O** and **Rb2·4H$_2$O**−**Rb7·4H$_2$O** were disordered. The central oxygen atom of the pop ligands in **K5·4H$_2$O** and **Rb5·2H$_2$O** and the terminal oxygen atom of the pop ligands in **K7·4H$_2$O** were disordered. Finally, the lattice water molecules in **K4·4H$_2$O**, **K5·4H$_2$O**, **Rb4·4H$_2$O**, and **Rb5·2H$_2$O** were disordered.

Although data collection was performed at 100 K in general, it was performed at 250 K for **K3·4H$_2$O** and **Rb3·4H$_2$O** and at 293 K for **K5·4H$_2$O** and **Rb5·2H$_2$O** to avoid the twinning observed at low temperature. In the X-ray oscillation photographs of **K7·4H$_2$O** and **Rb7·4H$_2$O**, very weak superlattice reflections corresponding to (h/2 k/2 l/2) were observed. However, since analysis including these reflections did not produce good results (R value was too large), we excluded these reflections in the analyses.

X-ray Powder Diffraction Measurements. X-ray powder diffraction (XRD) patterns were acquired on a Rigaku RINT 2500 diffractometer (50 kV 300 mA) with graphite-monochromated Cu Kα radiation (Kα1 λ = 1.5406 Å, Kα2 λ = 1.5444 Å) at room temperature. The samples were put into a glass capillary (ϕ = 0.5 or 0.8 mm). Diffraction data were collected in the range of 3.0° ≤ 2θ ≤ 60.0°. Sampling and scan widths were 0.02° and 0.1°/min, respectively. Raw data were analyzed by using RINT2000/PC software. The powder patterns were fitted using the Re Bail method as implemented in the program Rietica.[24]

Optical Conductivity Spectroscopy. Polarized reflectivity spectra were obtained by using a specially designed spectrometer with a 25 cm grating monochromator and an optical microscope. The obtained reflectivity spectra were converted to optical conductivity spectra using the Kramers−Kronig transformation.

Polarized Raman Spectroscopy. Polarized Raman spectra were acquired on a Renishaw Raman spectrometer with a continuous-wave He−Ne laser (1.96 eV) and an optical microscope. An optical cryostat (Iwatani GAS, Mini Stat) was used for the measurement at 30 K.

Electrical Conductivity Measurements. Direct current (DC) electrical conductivity measurements were performed in a liquid He cryostat of a Quantum Design PPMS (Physical Property Measuring System) MODEL 6000 by using two-probe method with a source-meter Keithley model 2611. Gold wires (15 μm ϕ) were attached to the sample stage parallel to the chain axis of the crystal with carbon paste (Dotite XC-12 in diethyl succinate), which covered the entire plane to obtain a homogeneous current density.

RESULTS AND DISCUSSION

Conditions for the Formation of MMX Chains with Binary Countercations. The general formula for the MMX chains with binary countercations is $A_2B[Pt_2(pop)_4I]\cdot nH_2O$ (A^+ = K^+ and Rb^+; B^{2+} = $\mathbf{1}^{2+}$−$\mathbf{7}^{2+}$; n = 2 and 4). A^+, which is coordinated by eight oxygen atoms, links both intra- and interchain $[Pt_2(pop)_4]$ units via $A^+\cdots O$ coordination bonds. B^{2+} link interchain $[Pt_2(pop)_4]$ units by $N^+-H\cdots O$ hydrogen bonds.

Li^+, Na^+, and Cs^+ could not be used because of their ionic radii. The eight-coordinate ionic radii of Li^+, Na^+, K^+, Rb^+, and Cs^+ are 1.06, 1.32, 1.65, 1.75, and 1.88 Å, respectively.[25] In the case of Li^+ and Na^+, which have small ionic radii, steric hindrance among the oxygen atoms around the alkali metal ions interferes with the formation of the 1D chain structure, which is consistent with the fact that $Li_4[Pt_2(pop)_4I]\cdot 4H_2O$ and $Na_4[Pt_2(pop)_4I]\cdot 2H_2O$ crystallize from concentrated solutions.[12e,26] We could not find any conditions under which Li^+ or Na^+ could be introduced as one of the countercations. In contrast, because of smaller steric hindrance around the larger Cs^+, only $Cs_4[Pt_2(pop)_4I]$ was obtained under the conditions we tried.

Only B^{2+} having three to five atoms in the main backbone between the terminal NH_3^+ groups could be introduced. The selectivity toward B^{2+} can be explained as follows. B^{2+} are located in the space surrounded by four $[Pt_2(pop)_4]$ units, which are connected via $A^+\cdots O$ coordination bonds (e.g., **K6·4H$_2$O** in Figure 1). Because the length of the coordination bonds is limited, the size of the space is also limited. Thus, longer aliphatic diammonium ions, such as $H_3NC_6H_{12}NH_3^{2+}$, cannot be introduced as one of the binary countercations. Similarly, shorter aliphatic diammonium ions, such as $H_3NC_2H_4NH_3^{2+}$, cannot form a hydrogen-bonding network

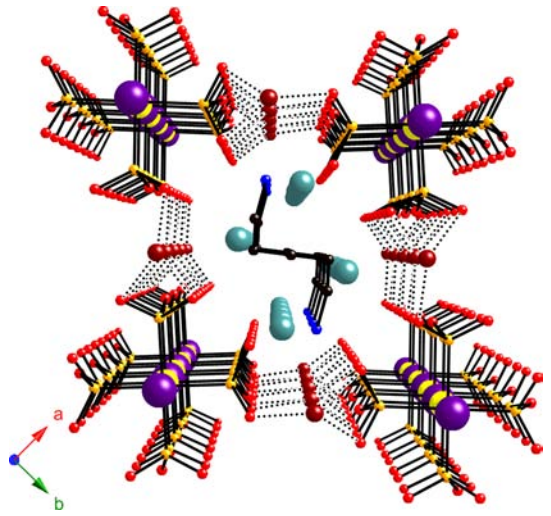

Figure 1. Perspective view of the region around $\mathbf{6}^{2+}$ along the c-axis of **K6·4H$_2$O** (black, C; blue, N; red, O(ligand); light blue, O(H_2O); orange, P; brown, K; purple, I; yellow, Pt). $K^+\cdots O$(ligand) coordination bonds are represented as dotted lines. Hydrogen atoms are omitted for clarity.

dx.doi.org/10.1021/ic301469u | Inorg. Chem. 2012, 51, 9967−9977

Table 2. Ratio of Unit Cell Parameters (b/a), Selected Bond Distances[a], Angles,[a] and Interatomic Distances[a] for MMX Chains with Binary Countercations

	b/a	d(Pt−I−Pt)/Å	d(Pt−I)/Å	d(Pt···I)/Å	d(A−O(ligand))/Å	∠(O−A−O)/deg	d(A···O(ligand))/Å
K1·4H$_2$O	1.09	5.6305(8)	2.641(3)	2.990(3)	2.822(8), 2.836(8)	83.4(3), 86.6(4)	3.981, 4.355
		5.9786(9)	2.828(6)	3.151(6)	2.777(8)−2.985(8)	86.4(3)−121.8(3)	
K2·4H$_2$O	1	5.7179(11)	2.7496(8)	2.9683(8)	2.856(3), 2.865(3)	86.95(8)	4.112, 4.340
		5.9254(11)	2.7993(7)	3.1261(8)	2.791(3)−3.007(3)	87.32(7)−121.18(7)	
K3·4H$_2$O	1	5.7262(11)	2.755(2)	2.951(2)	2.879(6)−2.882(7)	86.38(15)	4.169, 4.317
		5.9403(12)	2.8082(18)	3.1320(18)	2.827(7)−3.003(8)	87.78(15), 121.08(16)	
K4·4H$_2$O	1.20	5.7625(18)	2.7430(9)	3.0195(10)	2.7780(10)−3.0349(11)	87.04(4)−98.59(4)	3.706
K5·4H$_2$O	1.25	5.7921(11)	2.732(3)	3.060(3)	2.835(3)−3.054(3)	87.92(11)−98.55(11)	3.847
K6·4H$_2$O	1.19	5.7225(7)	2.729(9)	2.993(6)	2.791(2)−3.049(2)	81.93(10)−93.89(9)	3.949
K7·4H$_2$O	1.26	5.7244(11)	2.8757(6)		2.808(5)−3.22(2)	82.95(19)−100.9(7)	4.070
Rb1·4H$_2$O	1.10	5.7521(5)	2.7430(3)	3.0091(4)	2.8900(17)−2.9749(19)	83.90(5), 86.47(5)	4.001−4.542
		6.1928(5)	2.8217(3)	3.3710(3)	2.9009(17)−3.0551(17)	88.97(4)−127.84(4)	
Rb2·4H$_2$O	1	5.7782(7)	2.7478(5)	3.0304(4)	2.9387(17), 2.9484(15)	86.43(4)	4.146, 4.432
		6.1226(7)	2.8073(4)	3.3152(5)	2.9105(15)−3.0740(16)	89.54(4)−123.52(4)	
Rb3·4H$_2$O	1	5.7726(13)	2.7532(16)	3.0194(15)	2.961(6)−2.962(7)	86.00(14)	4.222, 4.417
		6.1518(13)	2.8155(16)	3.3363(16)	2.944(7)−3.080(7)	90.38(14)−124.38(13)	
Rb4·4H$_2$O	1.21	5.8554(15)	2.735(5)	3.120(4)	2.858(8)−3.112(9)	88.7(3)−97.6(3)	3.745
Rb5·2H$_2$O	1.26	5.7930(9)	2.8965(4)		2.913(5)−3.094(5)	81.4(2)−97.8(2)	3.659
Rb6·4H$_2$O	1.20	5.8219(15)	2.742(3)	3.080(3)	2.908(3)−3.089(3)	82.80(13)−96.41(12)	3.940
Rb7·4H$_2$O	1.27	5.823(2)	2.740(4)	3.097(4)	2.829(5)−3.214(6)	88.12(17)−94.75(19)	3.899

[a]The values related to the same Pt−I−Pt bond are listed in the same line.

among the pop ligands, and thus, MMX chains with binary countercations do not form.

Electronic States of MMX Chains with Binary Countercations. It is known that the distance between the bridging halide ions and metal ions in MX and MMX chains (d(M-X)) becomes shorter as the oxidation number of the metal becomes higher. In other words, the electronic state can be determined from the chain structure.

As shown in Table 2, there were two different Pt−I−Pt distances (d(Pt−I−Pt)) in **Rb1·4H$_2$O**−**Rb3·4H$_2$O**, indicating that they are in ACP states. However, they are not in simple ACP states because the Pt−I distances are shorter in one [Pt$_2$(pop)$_4$] unit (d(Pt−I)) than those in the other (d(Pt···I)), which is characteristic of CDW states. The structure is isomorphic to those of **K2·4H$_2$O**[14] and **K3·4H$_2$O**;[13] that is, **Rb1·4H$_2$O**−**Rb3·4H$_2$O** are in ACP+CDW states. In addition, the intradimer Pt−Pt distance (d(Pt−Pt)) reflects the oxidation state of Pt−Pt dimer.[27] Since d(Pt−Pt) of nonbonding Pt(II)$_2$ complex, K$_4$[Pt$_2$(pop)$_4$]·2H$_2$O (2.925(1) Å)[28] is longer than that of bonding Pt(III)$_2$ complex, K$_4$[Pt$_2$(pop)$_4$I$_2$] (2.754(1) Å),[29] the longer and shorter d(Pt−Pt) of **Rb1·4H$_2$O**−**Rb3·4H$_2$O** (Table 3) correspond to lower and higher oxidized Pt−Pt dimer, respectively. These data support the existence of CDW-like distortion. Moreover, the bridging iodide ions of **K2·4H$_2$O**, **K3·4H$_2$O**, and **Rb1·4H$_2$O**−**Rb3·4H$_2$O** are three-dimensionally ordered, which is very rare in MMX chains.[30]

Apparently, other compounds are also in a mixed-valent state because their d(Pt−Pt) were comparable to those of the mixed-valent Pt(II)−Pt(III) complexes reported so far.[12,31] Except for **K7·4H$_2$O** and **Rb5·2H$_2$O**, there were two different Pt−I distances because of disorder in the bridging iodide ions without ACP-like distortions. The origin of the disorder is the random arrangement of the 1D chains (Supporting Information, Figure S2), which makes it impossible to distinguish between the CDW and CP states via structural analysis. In the cases of **K7·4H$_2$O** and **Rb5·2H$_2$O**, although there was only one Pt−I distance in the crystal structure, it is possible that the resolution is less than the Pt−I distance. Therefore, spectroscopic studies are necessary for determining the electronic states of **K4·4H$_2$O**−**K7·4H$_2$O** and **Rb4·4H$_2$O**−**Rb7·4H$_2$O**.

Table 3. Intra-Dimer Pt−Pt Distance (d(Pt−Pt)) for MMX Chains with Binary Countercations

complexes	d(Pt−Pt)/Å	ref.
K1·4H$_2$O	2.8096(6)	13
K2·4H$_2$O	2.7469(6), 2.8668(6)	14
K3·4H$_2$O	2.7565(11), 2.8623(10)	13
K4·4H$_2$O	2.8227(9)	this work
K5·4H$_2$O	2.8326(6)	this work
K6·4H$_2$O	2.8179(4)	this work
K7·4H$_2$O	2.8138(7)	this work
Rb1·4H$_2$O	2.7554(3), 2.8720(3)	this work
Rb2·4H$_2$O	2.7472(4), 2.8825(4)	this work
Rb3·4H$_2$O	2.7479(10), 2.8825(10)	this work
Rb4·4H$_2$O	2.8382(12)	this work
Rb5·2H$_2$O	2.8369(7)	this work
Rb6·4H$_2$O	2.8335(8)	this work
Rb7·4H$_2$O	2.8267(11)	this work

Raman spectroscopy is a powerful tool for investigating the electronic states of MX and MMX chains and other mixed valence compounds.[12b,c,32] The peaks for the symmetric stretching mode of the Pt−Pt bond are observed at ∼100 cm^{-1}. Since there are two different Pt−Pt bonds, Pt^{3+}-Pt^{3+} and Pt^{2+}-Pt^{2+}, in the CDW state, two peaks appear in the polarized Raman spectra. On the other hand, there is only a Pt^{2+}-Pt^{3+} bond in the CP state, and thus, only one peak is observed in the CP state. As shown in Supporting Information, Figure S3 and Table S1, two peaks were observed at ∼100 cm^{-1} in the polarized Raman spectra of all of the present complexes, except for **Rb4·4H$_2$O**, whose crystal was too small to measure the spectrum. Therefore, we concluded that **K4·4H$_2$O**−**K7·4H$_2$O** and **Rb5·2H$_2$O**−**Rb7·4H$_2$O** were in CDW states. Moreover,

dx.doi.org/10.1021/ic301469u | Inorg. Chem. 2012, 51, 9967−9977

two peaks in the spectra of **Rb1·4H$_2$O**−**Rb3·4H$_2$O** indicated that there was a CDW-like distortion in the ACP+CDW state. Since d(Pt−I−Pt) of **Rb4·4H$_2$O** is in the region of the CDW state on the basis of a reported phase diagram[12f] and since **Rb4·4H$_2$O** is isomorphic to **K4·4H$_2$O**, which is in a CDW state, we believe that **Rb4·4H$_2$O** is in a CDW state.

Origin of an ACP-Like Distortion in the ACP+CDW State. As mentioned above, MMX chains containing $\mathbf{1}^{2+}$−$\mathbf{3}^{2+}$, that is, **K1·4H$_2$O**−**K3·4H$_2$O** and **Rb1·4H$_2$O**−**Rb3·4H$_2$O**, are in ACP+CDW states. The other MMX chains with binary countercations, which contain longer B^{2+}, are in CDW states. To realize new electronic states for MMX chains, the mechanism for the ACP-like distortion must be determined.

From the detailed crystal structure of the present complexes, B^{2+} are mainly arranged along the b-axis in the orthorhombic crystals, except in the tetragonal crystals of **K2·4H$_2$O**, **K3·4H$_2$O**, **Rb2·4H$_2$O**, and **Rb3·4H$_2$O**, resulting in the b-axes being longer than the a-axes. Table 2 shows the ratio of b/a for each MMX chains with binary countercations. The electronic state is an ACP+CDW state when $b/a \leq 1.10$ and is a CDW state when $b/a \geq 1.19$. A small b/a indicates steric hindrance around the A^+, which is explained as follows. Crystal structures of **K1·4H$_2$O** and **K6·4H$_2$O** viewed along the c-axis are shown in Figure 2. In each compound, ten oxygen atoms, eight from

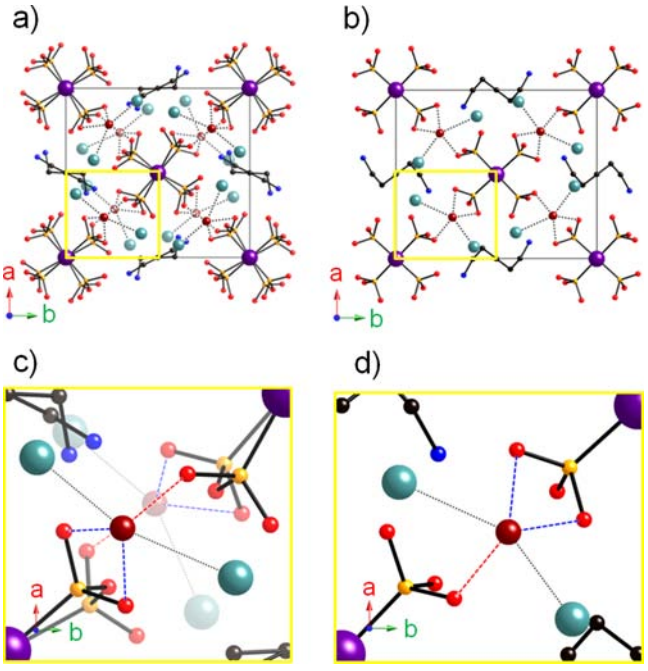

Figure 2. Crystal structures of (a,c) **K1·4H$_2$O** and (b,d) **K6·4H$_2$O**. (c) and (d) are magnifications of the yellow regions in (a) and (b), respectively (black, C; blue, N; red, O(ligand); light blue, O(H$_2$O); orange, P; brown, K; purple, I; yellow, Pt). In (c) and (d), K$^+$···O(ligand) coordination bonds are represented as red (monodentate mode) and blue (bidentate mode) dashed lines, and K$^+$···O(H$_2$O) coordination bonds are represented as black dotted lines. Hydrogen atoms are omitted for clarity.

the pop ligands (O(ligand)) and two from lattice H$_2$O molecules (O(H$_2$O)), are present around the A^+. When $b/a \leq 1.10$ corresponding to **K1·4H$_2$O**, the pop ligands in [Pt$_2$(pop)$_4$] unit twist, moving two O(ligand) atoms away from the A^+ because at most eight oxygen atoms can coordinate to the A^+. On the other hand, when $b/a \geq 1.19$ corresponding to **K6·4H$_2$O**, two O(ligand) atoms are far from the A^+ without twisting of the ligands in the [Pt$_2$(pop)$_4$] unit. The distance between the A^+ and the coordinated O(ligand) atoms (d(A-O(ligand))) and the A^+ and the other O(ligand) atoms (d(A···O(ligand))) are shown in Table 2. Since d(A···O-(ligand)) is longer than the sum of the ionic radii of A^+ (1.65 Å for K^+ and 1.75 Å for Rb^+)[25] and the van der Waals radii of the O atoms (1.52 Å),[33] no coordination bond exist between them. Because of the twisting of the pop ligands, the intrachain [Pt$_2$(pop)$_4$] units are linked via A^+ in **K1·4H$_2$O** in alternating mono- and bidentate coordination modes, as shown in Figure 3a (red and blue bonds, respectively). d(Pt−I−Pt) is different for each coordination mode.

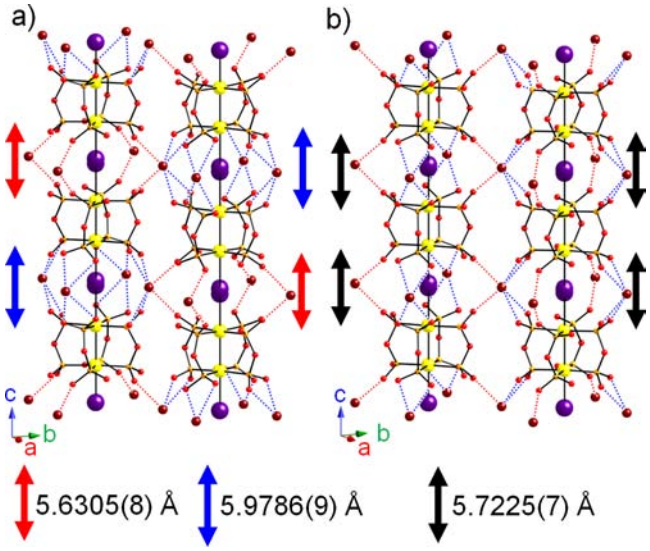

Figure 3. Chain structures of (a) **K1·4H$_2$O** and (b) **K6·4H$_2$O** with K$^+$···O(ligand) coordination bonds indicated with red (monodentate mode) and blue (bidentate mode) dotted lines (red, O(ligand); orange, P; brown, K; purple, I; yellow, Pt). B^{2+}, O(H$_2$O), and hydrogen atoms are omitted for clarity. Bridging iodide is disordered.

On the other hand, in **K6·4H$_2$O**, which is in a CDW state, intrachain [Pt$_2$(pop)$_4$] units are linked via the A^+ ions in mixed coordination modes consisting of monodentate and bidentate coordination modes equally (Figure 3b), resulting in a single d(Pt−I−Pt). Therefore, two types of d(Pt−I−Pt) observed in **K1·4H$_2$O** are induced by the twisting of the pop ligands, causing in the mixing of the ACP-like distortion into the CDW state.

Optical Conductivity Spectroscopy. To determine the electronic structure of the MMX chains with binary countercations in detail, we acquired polarized reflectance spectra (Supporting Information, Figure S4, S5) and transformed them to optical conductivity spectra by using the Kramers−Kronig relation. This measurement was performed on samples with clean surface areas larger than 0.1 × 0.1 mm^2. Figure 4 shows a spectrum for **K6·4H$_2$O** as an example. The spectra of the other complexes are shown in Supporting Information, Figures S6 and S7. Peak photon energies in these spectra are summarized in Table 4.

In the optical conductivity spectra of the MMX chains with binary countercations, a strong low energy charge transfer (CT) band at ∼1 eV and weak bands over 2 eV were observed. We have previously reported that the peak photon energy of the lowest CT band (E_{CT}) increases with an increase in the

dx.doi.org/10.1021/ic301469u | Inorg. Chem. 2012, 51, 9967−9977

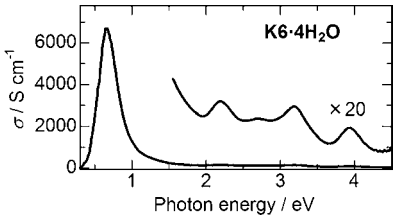

Figure 4. Optical conductivity spectrum of **K6·4H$_2$O** with the polarized light parallel to the *c* axis at room temperature.

Table 4. Peak Photon Energies in Optical Conductivity Spectra of the Present MMX Chains

complex	electronic state	photon energy/eV
K1·4H$_2$O	ACP+CDW	0.85, 2.15, 3.25, 3.95
K2·4H$_2$O	ACP+CDW	0.85, 2.23, 3.30, 3.83
K3·4H$_2$O	ACP+CDW	0.89, 2.28, 3.26, 3.9
K4·4H$_2$O	CDW	0.79, 2.22, 3.18, 3.91
K5·4H$_2$O	CDW	0.81, 2.22, 3.19, 3.92
K6·4H$_2$O	CDW	0.64, 2.19, 3.18, 3.94
Rb1·4H$_2$O	ACP+CDW	1.14, 2.13, 3.29, 3.86
Rb2·4H$_2$O	ACP+CDW	1.14, 2.2, 3.29, 3.80
Rb3·4H$_2$O	ACP+CDW	1.12, 2.2, 3.27, 3.78
Rb5·2H$_2$O	CDW	0.94, 2.16, 3.18, 3.80
Rb7·4H$_2$O	CDW	0.92, 2.15, 3.19, 3.82

d(Pt−I−Pt) in the CDW and CP states of pop-type MMX chains. In addition, the dependency of E_{CT} on *d*(Pt−I−Pt) in the CDW state is larger than that in the CP state because the interdimer CT in the CDW state is more sensitive to *d*(Pt−I−Pt) than the intradimer CT is in the CP state. This dependence of E_{CT} on *d*(Pt−I−Pt) has been plotted in relation to the CDW and CP states.[12f] Figure 5 shows a phase diagram for already-

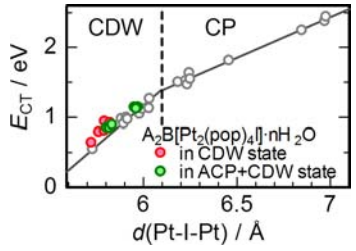

Figure 5. Phase diagram for already-known pop-type MMX chains (gray) plotted with data points for the MMX chains with binary countercations. The solid line was fitted with the data for the already-known pop-type MMX chains in each phase.

known MMX chains together with data points for those in Table 4 (see Supporting Information, Figure S8 for details). It should be noted that the average value of the two different *d*(Pt−I−Pt) was used in the case of the ACP+CDW state since the effect of *d*(Pt−I−Pt) on the perturbation of the energy level of the Pt ions is averaged. MMX chains with binary countercations in Table 4 could be fitted in the CDW state, indicating that CT occurs from the electron-rich Pt dimer to the electron-poor Pt dimer in the ACP+CDW state as well as in the CDW state. The peak photon energies of the weak bands were similar to those of MMX chains in typical CDW states,[12f,g] indicating that the electronic structure in the ACP+CDW state is similar to that in the CDW state. These results are consistent with the fact that **K1·4H$_2$O** is diamagnetic.[13,34] From the previous theoretical[8d] and experimental[10d] reports, the weak bands at about 2.2 eV, 3.2 eV, and 3.9 eV are ascribed to the CT processes between the nearest-neighbor Pt and I sites, between the intradimer Pt sites, and between the next-nearest-neighbor Pt and I sites, respectively. The results show that we could control the introduction of an ACP-like lattice distortion into MMX chains by changing the length of B^{2+} with retention of the electronic structure of the CDW state.

Structural Features of MMX Chains with Binary Countercations. Compared with MMX chains with unitary countercations, those with binary countercations have two important structural features. One is "synchronized" packing. Typical MMX chains with unitary countercations, which link only intrachain [Pt$_2$(pop)$_4$] units, have an "alternating" packing (Figure 6a).[12h] On the other hand, in the case of the MMX

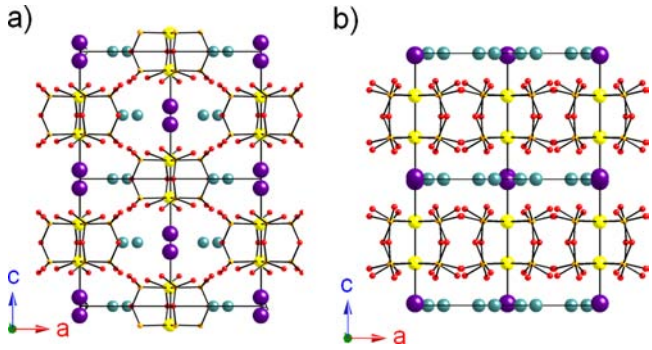

Figure 6. Crystal structures of (a) (**6**)$_2$[Pt$_2$(pop)$_4$I]·4H$_2$O[12h] and (b) **K6·4H$_2$O** (red, O(ligand); light blue, O(H$_2$O); orange, P; purple, I; yellow, Pt). Countercations and hydrogen atoms are omitted for clarity. The bridging iodides are disordered.

chains with binary countercations, the A^+ link not only intrachain but also interchain [Pt$_2$(pop)$_4$] units via A^+···O coordination bonds, and B^{2+} link interchain [Pt$_2$(pop)$_4$] units via N^+−H···O hydrogen bonds. The hydrogen bond and coordination bond networks constrain each [Pt$_2$(pop)$_4$] unit to arrange in the *ab* plane, causing a "synchronized" packing (Figure 6b). Because of the "synchronized" packing, the layer-like structure is perpendicular to the *c*-axis (chain axis). The [Pt$_2$(pop)$_4$] units and B^{2+} are located in the *ab* plane. Therefore, it is a densely packed layer. On the other hand, the loosely packed layer consists of the smaller iodide ions and A^+. H$_2$O molecules, which coordinate to A^+, fill the vacancies in the loosely packed layer. These H$_2$O molecules can be removed by dehydration.

The other important structural feature in the MMX chains with binary countercations is the short *d*(Pt−I−Pt) value. The reason for the short *d*(Pt−I−Pt) value can be explained as follows. In the case of the MMX chains with unitary countercations, the intrachain [Pt$_2$(pop)$_4$] units are linked via hydrogen bonds between the pop ligands and the NH_3^+ groups of the countercations, whereas in the case of MMX chains with binary countercations, they are linked via coordination bonds between the pop ligands and the A^+. The distances between the nitrogen atoms of the NH_3^+ moieties and O(ligand) atoms in the MMX chains with unitary countercations (Supporting Information, Table S2) and those between the A^+ and O(ligand) atoms in Table 2 are almost comparable (*d*(N−O) ≈ *d*(A−O)). However, the minimum values of the coordination bond angle (∠(O−A−O)) are smaller than those of the O(ligand)−NH$_3$−O(ligand) angles (∠(O−N−O)), resulting

dx.doi.org/10.1021/ic301469u | Inorg. Chem. 2012, 51, 9967−9977

in shorter d(Pt−I−Pt) in the MMX chains with binary countercations. This difference is due to the isotropic electron distribution in the A^+. In other words, the oxygen atoms can coordinate to the A^+ from any direction unless steric hindrance among the oxygen atoms occurs. In contrast, since ∠(H−N−H) for sp^3 hybridized N atoms is ∼109°, ∠(O−N−O) is larger than 109°. A comparison between $(\mathbf{6})_2[Pt_2(pop)_4I]\cdot 4H_2O$ and **K6·4H$_2$O** is shown in Supporting Information, Figure S9.

Although most of the pop-type MMX chains synthesized so far have low conductivities at room temperature ($\sigma_{RT} < 10^{-7}$ S cm^{-1}), the MMX chains with binary countercations should have higher electrical conductivities (σ) because of the short d(Pt−I−Pt).

Conducting Properties of MMX Chains with Binary Countercations. Figure 7 shows the relationship between

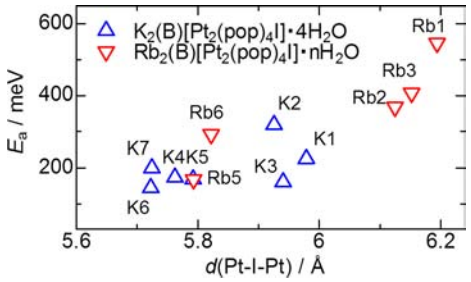

Figure 7. Relationship between d(Pt−I−Pt) and activation energy (E_a) of several MMX chains with binary countercations (shown as AB, which is the abbreviation of $A_2B[Pt_2(pop)_4I]\cdot nH_2O$) at high temperature.

d(Pt−I−Pt) and the activation energy (E_a) at high temperature obtained from the temperature dependence of σ of **K1·4H$_2$O−K7·4H$_2$O**, **Rb1·4H$_2$O−Rb3·4H$_2$O**, **Rb5·2H$_2$O**, and **Rb6·4H$_2$O** (Supporting Information, Figure S10 and Table S3). In the case of the ACP+CDW state, the longer value of d(Pt−I−Pt) was used because it should affect the hopping conduction in pop-type MMX chains.[12d] In this case, E_a became smaller as d(Pt−I−Pt) decreased. This trend has not been observed before for MMX chains. The σ_{RT} values of **K1·4H$_2$O−K7·4H$_2$O** were 10^{-2}−10^{-4} S cm^{-1} (Table 5, stage 1), which are the largest values reported so far for pop-type MMX chains.[12a,d]

Changes in Structure and σ of MMX Chains with Binary Countercations upon Dehydration. To determine the effect of B^{2+} upon dehydration−rehydration of the complex, we compared the changes in the structures and physical properties of **K4·4H$_2$O−K7·4H$_2$O** to those of the previously reported **K1·4H$_2$O−K3·4H$_2$O**.[13] XRD patterns were acquired at three stages: (1) initial hydrated complex, (2) after heating the initial complex at 70 °C at pressures <100 Pa for a day (dehydrated complex, **K4−K7**), and (3) after exposing the dehydrated complex to H_2O vapor for a day. Figure 8 shows

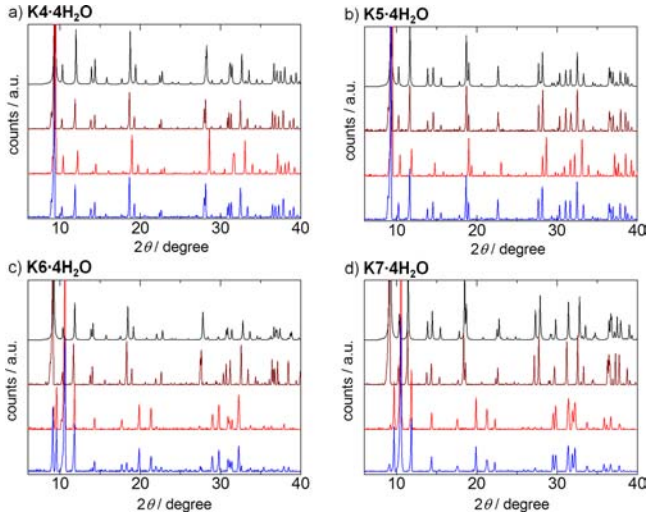

Figure 8. XRD patterns for (a) **K4·4H$_2$O**, (b) **K5·4H$_2$O**, (c) **K6·4H$_2$O**, and (d) **K7·4H$_2$O** simulated with the crystal structure (black) and measured for stages 1 (brown), 2 (red), and 3 (blue).

XRD patterns of **K4·4H$_2$O−K7·4H$_2$O** for each stage. **K4·4H$_2$O** and **K5·4H$_2$O** as well as **K1·4H$_2$O−K3·4H$_2$O**[13] underwent reversible structural changes. In contrast, the changes in **K6·4H$_2$O** and **K7·4H$_2$O** were irreversible. The XRD patterns in the stage 3 XRD spectra of **K6·4H$_2$O** were assigned to those for **K6** with minor patterns for **K6·4H$_2$O** (see Supporting Information, Figure S11), indicating that **K6** was slightly rehydrated. However, only the patterns for **K7** were observed in the stage 3 XRD spectra of **K7·4H$_2$O**. The XRD patterns of dehydrated **K4** and **K5**, which are isomorphic to **K1−K3**,[13] were fit with an orthorhombic C-lattice (Supporting Information, Figure S12 and Table S4). Values of d(Pt−I−Pt) in **K4** and **K5** were estimated to be close to that of **K1** because the lengths of the c axes were similar. However, the XRD patterns for **K6** and **K7** were quite different from those for **K6·4H$_2$O** and **K7·4H$_2$O**. Thus, detailed structural analyses of **K6** and **K7** are required.

The temperature dependence of σ parallel to the chain axis (c) of **K4·4H$_2$O−K7·4H$_2$O** for each stage is shown in Figures 9b−e with the data for **K1·4H$_2$O** (Figure 9a).[13] The conductivity of **K7·4H$_2$O** at stages 2 and 3 were unavailable because the value of σ was too small. Except for **K7·4H$_2$O**, E_a

Table 5. Electrical Conductivity at Room Temperature (298 K) (σ_{RT}) and the Activation Energy (E_a) at High Temperature of K1·4H$_2$O and K4·4H$_2$O−K7·4H$_2$O Measured at Three Stages[a]

	σ_{RT}/S cm^{-1}			E_a/meV		
initial complex	stage 1	stage 2	stage 3	stage 1	stage 2	stage 3
K1·4H$_2$O[13]	1.5×10^{-4}	1.4×10^{-3}	8.0×10^{-5}	226	122	196
K4·4H$_2$O	4.0×10^{-3}	1.0×10^{-3}	3.3×10^{-5}	174	122	151
K5·4H$_2$O	8.4×10^{-4}	9.4×10^{-3}	1.2×10^{-4}	169	96	195
K6·4H$_2$O	4.4×10^{-3}	1.6×10^{-4}	3.2×10^{-5}	145	126	148
K7·4H$_2$O	1.6×10^{-3}			200		

[a](1) Initial hydrated complex, (2) after heating the initial complex at 70 °C at pressures <100 Pa for a day (dehydrated complex), and (3) after exposing the dehydrated complex to H_2O vapor for a day.

dx.doi.org/10.1021/ic301469u | Inorg. Chem. 2012, 51, 9967−9977

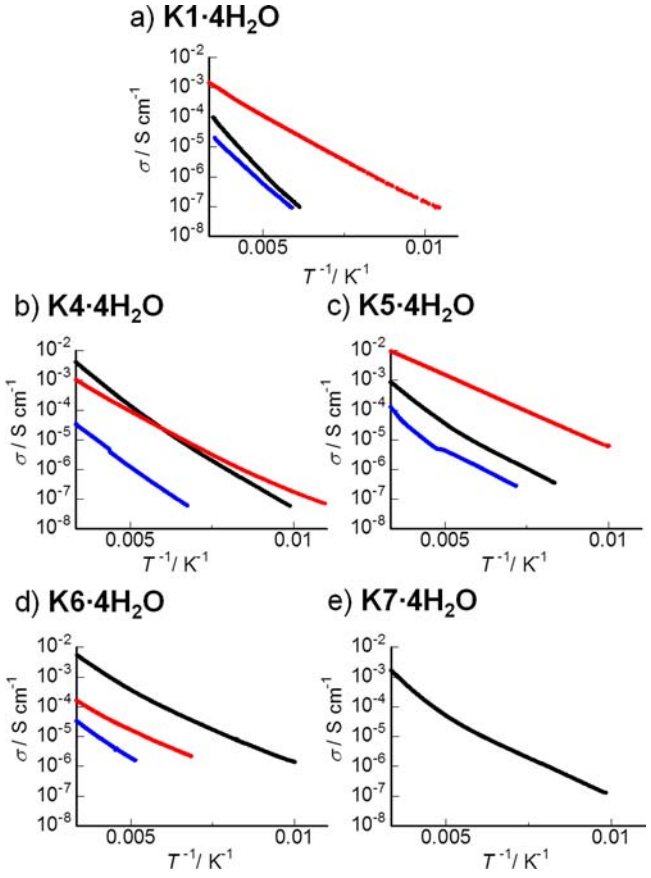

Figure 9. Temperature dependence of the electrical conductivity (σ) at stages 1 (black), 2 (red), and 3 (blue) of (a) **K1·4H$_2$O**,[13] (b) **K4·4H$_2$O**, (c) **K5·4H$_2$O**, (d) **K6·4H$_2$O**, and (e) **K7·4H$_2$O**.

decreased upon dehydration because of a decrease in d(Pt–I–Pt). Although a detailed structure of **K6** has not been obtained, the decrease in E_a suggests that the orbital overlap between the Pt ($5d_{z^2}$) and I ($5p_z$) ions increases upon dehydration.

The change in σ_{RT} upon dehydration and rehydration depends on the complex, as shown in Table 5. Although σ_{RT} of **K5** was 10 times larger than that of **K5·4H$_2$O**, σ_{RT} of **K4** and **K6** were 0.25 and 0.04 times larger than those of **K4·4H$_2$O** and **K6·4H$_2$O**, respectively. The lower values of σ_{RT} may be due to partial degradation of the sample, such as small cracks in the crystals, limiting the current flow in the crystal and, thus, reducing the effective cross-sectional area of the crystals. After exposure to water vapor, σ_{RT} decreased to 0.008, 0.14, and 0.007 times larger than those of the initial **K4·4H$_2$O–K6·4H$_2$O**, respectively. Since the crystal structures of **K4·4H$_2$O** and **K5·4H$_2$O** completely recovered as shown in Figure 8, the decrease may be due to the partial degradation of the sample. Moreover, slight rehydration of **K6** reduced the quality of the crystal. Degradation of the crystals of **K1·4H$_2$O–K3·4H$_2$O** during dehydration–rehydration was scarcely observed, as reported previously.[13] The values of σ_{RT} of **K1–K3** were 10–50 times larger than those of **K1·4H$_2$O–K3·4H$_2$O**, and they returned to almost those of the initial state upon rehydration. These results indicate that robustness of the MMX chains with binary countercations decreases in the following order: **K1·4H$_2$O–K3·4H$_2$O** > **K5·4H$_2$O** > **K4·4H$_2$O** > **K6·4H$_2$O** > **K7·4H$_2$O**.

In other words, the complexes with longer B^{2+} moieties have weaker frameworks. In **K1·4H$_2$O–K3·4H$_2$O**, the B^{2+} moieties are in almost zigzag conformations, whereas in **K4·4H$_2$O–K7·4H$_2$O**, the long B^{2+} moieties are in less-stable bent conformations (Supporting Information, Figure S13) because of less space, as mentioned above (Figure 1). We concluded that the differences in the stabilities of the B^{2+} ions caused the difference in the robustness of the complexes.

CONCLUSION

To determine the origin of the ACP+CDW state, which is a new electronic state for MMX-chain complexes,[13,14] and to determine the effects of the countercations on the physical properties and the dehydration–rehydration behavior of MMX chains, we synthesized a series of MMX chains with binary countercations, $A_2B[Pt_2(pop)_4I]\cdot nH_2O$ (A^+ = K^+ and Rb^+; B^{2+} = aliphatic diammonium ion; n = 2 and 4). Crystal structure analyses and polarized Raman spectra of these complexes clearly indicated that the complexes with short B^{2+}, $H_3NCH_2CHXCH_2NH_3^{2+}$ (X = H, Me, Cl), were in ACP +CDW states and that the MMX chains with longer B^{2+} were in CDW states. The ACP-like distortion in the ACP+CDW state is due to twisting of the pop ligands caused by steric hindrance around A^+. From optical conductivity spectra, the electronic structure of the ACP+CDW state is similar to that of the CDW state despite the presence of the ACP-like distortion. The "synchronized" packing and short d(Pt–I–Pt) greatly affect σ and dehydration–rehydration of the MMX chains with binary countercations. The values of σ indicate that E_a becomes smaller as d(Pt–I–Pt) shortens. The reversible changes in σ upon dehydration–rehydration process depend largely on the robustness of the frameworks, which decreases as the length of B^{2+} increases.

ASSOCIATED CONTENT

Supporting Information

Additional experimental details, including polarized Raman spectra, polarized reflectance spectra, optical conductivity spectra, temperature dependence of electrical conductivity, XRD patterns, and the results of fitting, and X-ray crystallographic information file in CIF format for **K4·4H$_2$O–K7·4H$_2$O** and **Rb1·4H$_2$O–Rb7·4H$_2$O**. This material is available free of charge via the Internet at http://pubs.acs.org.

AUTHOR INFORMATION

Corresponding Author

*E-mail: h-iguchi@mail.cstm.kyushu-u.ac.jp (H.I.), yamasita@agnus.chem.tohoku.ac.jp (M.Y.).

Present Addresses

[§]Department of Chemistry and Biochemistry, Graduate School of Engineering, Kyushu University, Fukuoka, 819–0395, Japan. [‖]Research Institute of Instrumentation Frontier, National Institute of Advanced Industrial Science and Technology (AIST), 1-1-1 Higashi, Tsukuba, Ibaraki 305-8565, Japan.

Author Contributions

The manuscript was written through contributions of all authors. All authors have given approval to the final version of the manuscript.

Notes

The authors declare no competing financial interest.

ACKNOWLEDGMENTS

This work was partly supported by a Grant-in-Aid for Creative Scientific Research from the Ministry of Education, Culture,

Sports, Science, and Technology (M.Y.), by a Grant-in-Aid by MEXT (No. 20110005 (H.O.)), by JSPS Research Fellowships for Young Scientists (H.I.), by the Global COE Program of Tohoku University (H.I.), and by the Tohoku University Institute for International Advanced Research and Education (H.I.).

REFERENCES

(1) (a) Ferraris, J. P.; Cowan, D. O.; Walatka, V. V.; Perlstein, J. H. *J. Am. Chem. Soc.* **1973**, *95*, 948−949. (b) Shirakawa, H.; Louis, E. J.; MacDiarmid, A. G.; Chiang, C. K.; Heeger, A. J. *J. Chem. Soc., Chem. Commun.* **1977**, 578−580.

(2) Sauteret, C.; Hermann, J.-P.; Frey, R.; Pradère, F.; Ducuing, J.; Baughman, R. H.; Chance, R. R. *Phys. Rev. Lett.* **1976**, *36*, 956−959.

(3) (a) Kishida, H.; Matsuzaki, H.; Okamoto, H.; Manabe, T.; Yamashita, M.; Taguchi, Y.; Tokura, Y. *Nature* **2000**, *405*, 929−932. (b) Tao, S.; Miyagoe, T.; Maeda, A.; Matsuzaki, H.; Ohtsu, H.; Hasegawa, M.; Takaishi, S.; Yamashita, M.; Okamoto, H. *Adv. Mater.* **2007**, *19*, 2707−2710.

(4) Bockrath, M.; Cobden, D. H.; Lu, J.; Rinzler, A. G.; Smalley, R. E.; Balents, L.; McEuen, P. L. *Nature* **1999**, *397*, 598−601.

(5) Iwai, S.; Okamoto, H. *J. Phys. Soc. Jpn.* **2006**, *75*, 011007−1−21.

(6) Okamoto, H.; Yamashita, M. *Bull. Chem. Soc. Jpn.* **1998**, *71*, 2023−2039.

(7) Takaishi, S.; Takamura, M.; Kajiwara, T.; Miyasaka, H.; Yamashita, M.; Iwata, M.; Matsuzaki, H.; Okamoto, H.; Tanaka, H.; Kuroda, S.; Nishikawa, H.; Oshio, H.; Kato, K.; Takata, M. *J. Am. Chem. Soc.* **2008**, *130*, 12080−12084.

(8) (a) Kuwabara, M.; Yonemitsu, K. *Mol. Cryst. Liq. Cryst.* **2000**, *341*, 533−538. (b) Kuwabara, M.; Yonemitsu, K. *Mol. Cryst. Liq. Cryst.* **2000**, *343*, 47−52. (c) Kuwabara, M.; Yonemitsu, K. *J. Phys. Chem. Solids* **2001**, *62*, 435−438. (d) Kuwabara, M.; Yonemitsu, K. *J. Mater. Chem.* **2001**, *11*, 2163−2175.

(9) (a) Robin, M. B.; Day, P. *Adv. Inorg. Chem. Radiochem.* **1967**, *9*, 247−422. (b) Day, P. *Low-dimensional cooperative phenomena*; Keller, H. J., Ed.; Plenum Press: New York, 1974; pp 191−214.

(10) (a) Bellitto, C.; Flamini, A.; Gastaldi, L.; Scaramuzza, L. *Inorg. Chem.* **1983**, *22*, 444−449. (b) Bellitto, C.; Dessy, G.; Fares, V. *Inorg. Chem.* **1985**, *24*, 2815−2820. (c) Clark, R. J. H.; Walton, J. R. *Inorg. Chim. Acta* **1987**, *129*, 163−171. (d) Kitagawa, H.; Onodera, N.; Sonoyama, T.; Yamamoto, M.; Fukawa, T.; Mitani, T.; Seto, M.; Maeda, Y. *J. Am. Chem. Soc.* **1999**, *121*, 10068−10080. (e) Mitsumi, M.; Murase, T.; Kishida, H.; Yoshinari, T.; Ozawa, Y.; Toriumi, K.; Sonoyama, T.; Kitagawa, H.; Mitani, T. *J. Am. Chem. Soc.* **2001**, *123*, 11179−11192. (f) Mitsumi, M.; Kitamura, K.; Morinaga, A.; Ozawa, Y.; Kobayashi, M.; Toriumi, K.; Iso, Y.; Kitagawa, H.; Mitani, T. *Angew. Chem., Int. Ed.* **2002**, *41*, 2767−2771. (g) Otsubo, K.; Kobayashi, A.; Kitagawa, H.; Hedo, M.; Uwatoko, Y.; Sagayama, H.; Wakabayashi, Y.; Sawa, H. *J. Am. Chem. Soc.* **2006**, *128*, 8140−8141. (h) Mitsumi, M.; Yoshida, Y.; Kohyama, A.; Kitagawa, Y.; Ozawa, Y.; Kobayashi, M.; Toriumi, K.; Tadokoro, M.; Ikeda, N.; Okumura, M.; Kurmoo, M. *Inorg. Chem.* **2009**, *48*, 6680−6691. (i) Mitsumi, M.; Yamashita, T.; Aiga, Y.; Toriumi, K.; Kitagawa, H.; Mitani, T.; Kurmoo, M. *Inorg. Chem.* **2011**, *50*, 4368−4377.

(11) (a) Welte, L.; Garcia-Couceiro, U.; Castillo, O.; Olea, D.; Polop, C.; Guijarro, A.; Luque, A.; Gomez-Rodriguez, J. M.; Gomez-Herrero, J.; Zamora, F. *Adv. Mater.* **2009**, *21*, 2025−2028. (b) Welte, L.; Calzolari, A.; Felice, R. D.; Zamora, F.; Gomez-Herrero, J. *Nat. Nanotechnol.* **2010**, *5*, 110−115. (c) Guijarro, A.; Castillo, O.; Welte, L.; Calzolari, A.; Miguel, P. J. S.; Gomez-Garcia, C. J.; Olea, D.; Felice, R. D.; Gomez-Herrero, J.; Zamora, F. *Adv. Funct. Mater.* **2010**, *20*, 1451−1457. (d) Mas-Balleste, R.; Gomez-Herrero, J.; Zamora, F. *Chem. Soc. Rev.* **2010**, *39*, 4220−4233.

(12) (a) Che, C.-M.; Herbstein, F. H.; Schaefer, W. P.; Marsh, R. E.; Gray, H. B. *J. Am. Chem. Soc.* **1983**, *105*, 4604−4607. (b) Kurmoo, M.; Clark, R. J. H. *Inorg. Chem.* **1985**, *24*, 4420−4425. (c) Clark, R. J. H.; Kurmoo, M.; Dawes, H. M.; Hursthouse, M. B. *Inorg. Chem.* **1986**, *25*, 409−412. (d) Butler, L. G.; Zietlow, M. H.; Che, C.-M.; Schaefer, W. P.; Sridhar, S.; Grunthaner, P. J.; Swanson, B. I.; Clark, R. J. H.; Gray, H. B. *J. Am. Chem. Soc.* **1988**, *110*, 1155−1162. (e) Yamashita, M.; Miya, S.; Kawashima, T.; Manabe, T.; Sonoyama, T.; Kitagawa, H.; Mitani, T.; Okamoto, H.; Ikeda, R. *J. Am. Chem. Soc.* **1999**, *121*, 2321−2322. (f) Matsuzaki, H.; Matsuoka, T.; Kishida, H.; Takizawa, K.; Miyasaka, H.; Sugiura, K.; Yamashita, M.; Okamoto, H. *Phys. Rev. Lett.* **2003**, *90*, 046401−1−4. (g) Mastuzaki, H.; Kishida, H.; Okamoto, H.; Takizawa, K.; Matsunaga, S.; Takaishi, S.; Miyasaka, H.; Sugiura, K.; Yamashita, M. *Angew. Chem., Int. Ed.* **2005**, *44*, 3240−3243. (h) Yamashita, M.; Takizawa, K.; Matsunaga, S.; Kawakami, D.; Iguchi, H.; Takaishi, S.; Kajiwara, T.; Iwahori, F.; Ishii, T.; Miyasaka, H.; Sugiura, K.; Matsuzaki, H.; Kishida, H.; Okamoto, H. *Bull. Chem. Soc. Jpn.* **2006**, *79*, 1404−1406. (i) Iguchi, H.; Takaishi, S.; Kajiwara, T.; Miyasaka, H.; Yamashita, M.; Matsuzaki, H.; Okamoto, H. *J. Inorg. Organomet. Polym. Mater.* **2009**, *19*, 85−90. (j) Iguchi, H.; Jiang, D.; Xie, J.; Takaishi, S.; Yamashita, M. *Polymers* **2011**, *3*, 1652−1661.

(13) Iguchi, H.; Takaishi, S.; Miyasaka, H.; Yamashita, M.; Matsuzaki, H.; Okamoto, H.; Tanaka, H.; Kuroda, S. *Angew. Chem., Int. Ed.* **2010**, *49*, 552−555.

(14) Iguchi, H.; Takaishi, S.; Kajiwara, T.; Miyasaka, H.; Yamashita, M.; Matsuzaki, H.; Okamoto, H. *J. Am. Chem. Soc.* **2008**, *130*, 17668−17669.

(15) (a) Che, C.-M.; Butler, L. G.; Gray, H. B. *J. Am. Chem. Soc.* **1981**, *103*, 7796−7797. (b) Kimura, N.; Ohki, H.; Ikeda, R.; Yamashita, M. *Chem. Phys. Lett.* **1994**, *220*, 40−45.

(16) Lin, J.; Pittman, C. U., Jr. *J. Organomet. Chem.* **1996**, *512*, 69−78.

(17) Appleton, T. G.; Hall, J. R. *Inorg. Chem.* **1972**, *11*, 112−117.

(18) He, Z.; Nadkarni, D. V.; Sayre, L. M.; Greenway, F. T. *Biochim. Biophys. Acta* **1995**, *1253*, 117−127.

(19) Anelli, P. L.; Montanari, F.; Quici, S. *J. Org. Chem.* **1985**, *50*, 3453−3457.

(20) *SMART (Version 5.611) and SAINT (Version 6.02). Area Detector Control and Integration Software*; Bruker AXS: Madison, WI, 1999.

(21) Altomare, A.; Burla, M. C.; Camalli, M.; Cascarano, G. L.; Giacovazzo, C.; Guagliardi, A.; Moliterni, A.G. G.; Polidori, G.; Spagna, R. *J. Appl. Crystallogr.* **1999**, *32*, 115−119.

(22) Sheldrick, G. M. *Acta Crystallogr.* **2008**, *A64*, 112−122.

(23) Wakita, K. *Yadokari-XG, Software for Crystal Structure Analyses*; 2001; Release of Software (Yadokari-XG 2009) for Crystal Structure Analyses, Kabuto, C.; Akine, S.; Nemoto, T.; Kwon, E. *J. Crystallogr. Soc. Jpn.* **2009**, *51*, 218−224.

(24) Howard, C. J.; Hunter, B. A. *Rietica, a Computer Program for Rietveld Analysis of X-Ray and Neutron Powder Diffraction Patterns*; Lucas Heights Research Laboratories: NSW, Australia, 1998; pp 1−27.

(25) Shannon, R. D. *Acta Crystallogr.* **1976**, *A32*, 751−767.

(26) Kawashima, T.; Miya, S.; Manabe, T.; Yamashita, M.; Takizawa, K.; Ishii, T.; Matsuzaka, H.; Sonoyama, T.; Kitagawa, H.; Mitani, T.; Matsuzaki, H.; Kishida, H.; Okamoto, H.; Ikeda, R. *Mol. Cryst. Liq. Cryst.* **2000**, *343*, 145−150.

(27) Roundhill, D. M.; Gray, H. B.; Che, C.-M. *Acc. Chem. Res.* **1989**, *22*, 55−61.

(28) (a) Dos Remedios Pinto, M. A.; Sadler, P. J.; Neidle, S.; Sanderson, M. R.; Subbiah, A.; Kuroda, R. *Chem. Commun.* **1980**, 13. (b) Marsh, R. E.; Herbstein, F. H. *Acta Crystallogr., Sect. B* **1983**, *39*, 280−287.

(29) Alexander, K. A.; Bryan, S. A.; Fronczek, F. R.; Fultz, W. C.; Rheingold, A. L.; Roundhill, D. M.; Stein, P.; Watkins, S. F. *Inorg. Chem.* **1985**, *24*, 2803−2808.

(30) Matsunaga, S.; Takizawa, K.; Kawakami, D.; Iguchi, H.; Takaishi, S.; Kajiwara, T.; Miyasaka, H.; Yamashita, M.; Matsuzaki, H.; Okamoto, H. *Eur. J. Inorg. Chem.* **2008**, 3269−3273.

(31) Bennett, M. A.; Bhargava, S. K.; Bond, A. M.; Bansal, V.; Forsyth, C. M.; Guo, S.-X.; Privér, S. H. *Inorg. Chem.* **2009**, *48*, 2593−2604.

(32) (a) Clark, R. J. H. *Chem. Soc. Rev.* **1984**, *13*, 219−244. (b) Clark, R. J. H. *Chem. Soc. Rev.* **1990**, *19*, 107−131.

(33) Bondi, A. *J. Phys. Chem.* **1964**, *68*, 441−452.

(34) Tanaka., H.; Kuroda, S.; Iguchi, H.; Takaishi, S.; Yamashita, M. *Phys. Rev. B* **2012**, *85*, 073104.